Available online at www.sciencedirect.com
ScienceDirect
Earth and Planetary Science Letters 261 (2007) 350–366
EPSL
www.elsevier.com/locate/epsl

# Diagenetic formation of greigite and pyrrhotite in gas hydrate marine sedimentary systems

Juan C. Larrasoaña [a,*], Andrew P. Roberts [b], Robert J. Musgrave [c], Eulàlia Gràcia [d], Elena Piñero [d], Marta Vega [c], Francisca Martínez-Ruiz [e]

[a] Institut de Ciències de la Terra Jaume Almera, CSIC, Lluís Solé Sabarís s/n, 08028 Barcelona, Spain
[b] National Oceanography Centre, Southampton, University of Southampton, European Way, Southampton SO14 3ZH, UK
[c] PALM Laboratory, School of Environmental and Life Sciences, University of Newcastle, Callaghan NSW 2308, Australia
[d] Unitat de Tecnologia Marina, CSIC, Centre Mediterrani d'Investigacions Marines i Ambientals, CSIC, Passeig Marítim de la Barceloneta 37–49, 08003 Barcelona, Spain
[e] Instituto Andaluz de Ciencias de la Tierra, CSIC-Universidad de Granada, Campus Fuentenueva, 18002 Granada, Spain

Received 21 February 2007; received in revised form 27 June 2007; accepted 27 June 2007
Available online 14 July 2007
Editor: M.L. Delaney

**Abstract**

Mineral magnetic results and electron microscope observations from gas hydrate-bearing marine sediments cored at southern Hydrate Ridge during Ocean Drilling Program Leg 204 (Sites 1244 to 1252, Cascadia Margin, offshore Oregon) demonstrate that authigenic greigite and pyrrhotite formed as a byproduct of microbially-mediated diagenetic reactions in the sulphate, the anaerobic oxidation of methane (AOM), and the methanic/gas hydrate zones. Geochemical conditions favourable for formation and preservation of greigite and pyrrhotite appear to be a limited source of sulphide, whether it derives from microbially-driven sulphate reduction in the sulphate zone, in the AOM zone or in deep sediments undergoing AOM, so that pyritization reactions are not driven to completion. Our results indicate that rock magnetic identification of greigite and pyrrhotite should be useful for detecting ancient gas hydrate systems in the marine sedimentary record, because it can enable rapid screening of ancient sediments for potential horizons where methane and disseminated gas hydrates might have occurred. Formation of authigenic greigite and pyrrhotite at different depths within the gas hydrate stability zone also implies that the magnetization of the host sediments will have been acquired at variable times, which is likely to compromise paleomagnetic results from greigite- and pyrrhotite-bearing marine sediments.


*Keywords:* mineral magnetism; greigite; pyrrhotite; iron sulphide; siderite; diagenesis; sulphate reduction; methane; anaerobic oxidation of methane; gas hydrate; marine sediments

## 1. Introduction

The importance of the two most common magnetic iron sulphide minerals, greigite ($Fe_3S_4$) and monoclinic pyrrhotite ($Fe_7S_8$), in marine sediments is being increasingly acknowledged. These minerals can form in association with microbially-mediated processes such as sulphate reduction (Liu et al., 2004), anaerobic oxidation of methane (AOM) (Kasten et al., 1998; Neretin et al., 2004; Jørgensen et al., 2004; Horng and Chen, 2006), and formation of gas hydrates (Housen and

* Corresponding author.
*E-mail address:* jclarra@ija.csic.es (J.C. Larrasoaña).

0012-821X/$ - see front matter © 2007 Elsevier B.V. All rights reserved.
doi:10.1016/j.epsl.2007.06.032

Musgrave, 1996; Musgrave et al., 2006; Larrasoaña et al., 2006). Beside providing significant sinks for the sulphur and iron cycles, sedimentary iron sulphides are also closely related to the dynamics of the carbon cycle, and their occurrence is relevant to the early evolution of life and to fueling of the deep biosphere (Schoonen et al., 2004; Pósfai and Dunin-Borkowski, 2006). Formation of magnetic iron sulphides can occur at any diagenetic stage from shallow burial to uplift and folding, with interstitial pore fluids that range from seawater to evolved orogenic fluids or hydrocarbons (Reynolds et al., 1994; Horng et al., 1998; Dinarès-Turell and Dekkers, 1999; Weaver et al., 2002; Liu et al., 2004; Kao et al., 2004; Roberts and Weaver, 2005; Rowan and Roberts, 2005; Sagnotti et al., 2005; Rowan and Roberts, 2006; Horng and Roberts, 2006). Therefore, unravelling their timing of formation

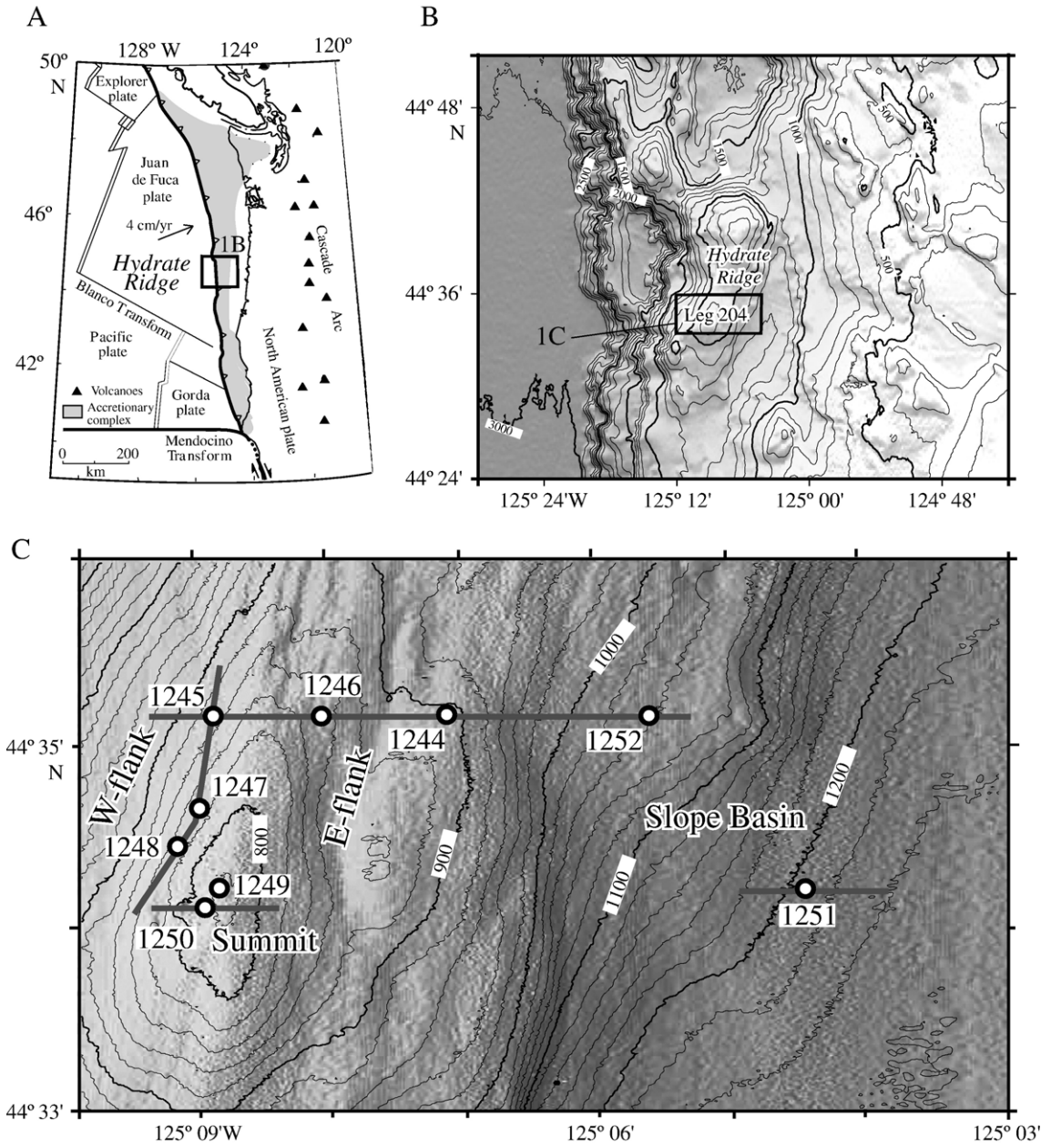


Fig. 1. A) Plate tectonic setting of the Cascadia convergent margin, with location of Hydrate Ridge. B) Bathymetric map of the Cascadia accretionary complex offshore Oregon, where Hydrate Ridge is located (contour interval = 100 m). C) Bathymetric map of southern Hydrate Ridge, with location of ODP Leg 204 sites 1244 to 1252 (contour interval = 20 m). Dark grey lines indicate the locations of multi-channel seismic sections shown in Fig. 2.

has implications for understanding the dynamics of biogeochemical cycles (Pósfai and Dunin-Borkowski, 2006) and for assessing the reliability of paleomagnetic data from marine sediments (Roberts and Weaver, 2005; Horng and Roberts, 2006).

Previous mineral magnetic studies of sediments from Hydrate Ridge (Cascadia Continental Margin, offshore Oregon) indicate the widespread occurrence of greigite (Housen and Musgrave, 1996; Musgrave et al., 2006; Larrasoaña et al., 2006), and maybe also of pyrrhotite (Larrasoaña et al., 2006), associated with gas hydrates. Greigite is interpreted to have formed in the strongly reducing conditions below the sulphate zone as a result of the metabolic activity of microorganisms (Housen and Musgrave, 1996; Musgrave et al., 2006), whose populations are enhanced in the presence of gas hydrate (Cragg et al., 1996). Greigite is preserved in the sediments, but gas hydrate eventually dissociates as sedimentation continues and/or as pressure and temperature conditions change, therefore the occurrence of greigite below the gas hydrate stability zone (GHSZ) has been proposed as a useful marker for the former presence of gas hydrates (Housen and Musgrave, 1996; Musgrave et al., 2006; Larrasoaña et al., 2006). This is important because dissociation of gas hydrates might have played a prominent role in driving global climate change and triggering large submarine landslides in the past (Kvenvolden, 1993).

In this paper, we present a detailed mineral magnetic study of sediments that were recovered from Sites 1244 to 1252 of Ocean Drilling Program (ODP) Leg 204 at southern Hydrate Ridge (SHR). We use published rock magnetic data (Larrasoaña et al., 2006) and new results to identify the specific magnetic iron sulphide minerals, to determine their microtextural relationship with other sediment constituents, and to establish the relative timing of their formation. Unravelling these issues is necessary to establish the mechanism(s) responsible for the formation of magnetic iron sulphides in the gas hydrate-bearing sediments of Hydrate Ridge. This is needed to determine the relevance of magnetic iron sulphides in the study of fossil gas hydrate marine sedimentary systems, and also to develop a robust understanding of their paleomagnetic significance in the geological record.

## 2. Geological setting

Hydrate Ridge is a structural ridge located offshore of Oregon (USA) in the Cascadia subduction zone, where the Juan de Fuca plate is being obliquely subducted beneath the North American plate at a rate of ~40 mm/yr (Fig. 1A) (Tréhu et al., 2003). During ODP Leg 204, nine sites were cored throughout the SHR (Tréhu et al., 2003) (Fig. 1B,C) (see Supplementary data, Table 1). SHR is composed of middle Pleistocene to Holocene (1.2–0 Ma) sedimentary units that are folded into an asymmetric anticline with a relatively steeply dipping western flank and a gently dipping eastern flank that links the summit of the ridge to the slope basin to the east (Tréhu et al., 2003, 2006) (Fig. 2). Beneath these units, older sediments (>1.2 Ma) constitute the accretionary complex of the subduction zone (Tréhu et al., 2003, 2006).

SHR sediments mainly consist of hemipelagic clays and silty clays that are locally interbedded with silty to sandy turbidite intervals often containing volcanic ash and glass (Tréhu et al., 2003, 2004b; Gràcia et al., 2006) (Fig. 3). Hemipelagic clays and silty clays are often speckled with millimetre-scale black nodules composed of iron sulphides (Tréhu et al., 2003) (Fig. 3C). This black speckling is locally associated with turbidite beds (Fig. 3B) and fracture planes that cut across bedding, sometimes including larger iron sulphide nodules (up to 1 cm long) that are strongly magnetic (Fig. 3D) (Tréhu et al., 2003). Sedimentological, geophysical, and geochemical data, together with direct sampling, indicate the occurrence of gas hydrates in the sediments of SHR (Tréhu et al., 2003, 2004a, 2006). Gas hydrates appear primarily in discrete lenses that are heterogeneously distributed. These lenses occur in clusters that are several metres thick and have orientations ranging from horizontal to vertical (Tréhu et al., 2003, 2004a, 2006). Gas hydrate contents vary from 1 to 8% throughout most of the GHSZ, except near methane vents at the summit of the ridge, where massive gas hydrates appear in the upper 20–40 m below seafloor (mbsf) and occupy 20–30% of the total volume of the sediment.

## 3. Methods

Identification of magnetic iron sulphides in sediments can be achieved using mineralogical techniques such as X-ray diffraction (XRD) (Roberts, 1995; Kasten et al., 1998; Neretin et al., 2004) and scanning electron microscopy (SEM) (Jiang et al., 2001; Weaver et al., 2002; Sagnotti et al., 2005; Roberts and Weaver, 2005; Rowan and Roberts, 2006), and magnetic methods such as thermal demagnetization of a composite isothermal remanent magnetization (IRM) (Lowrie, 1990), hysteresis experiments (Housen and Musgrave, 1996; Musgrave et al., 2006), and first-order reversal curve (FORC) diagrams (Roberts et al., 2000). Among bulk magnetic properties, the intensity of an IRM imparted to

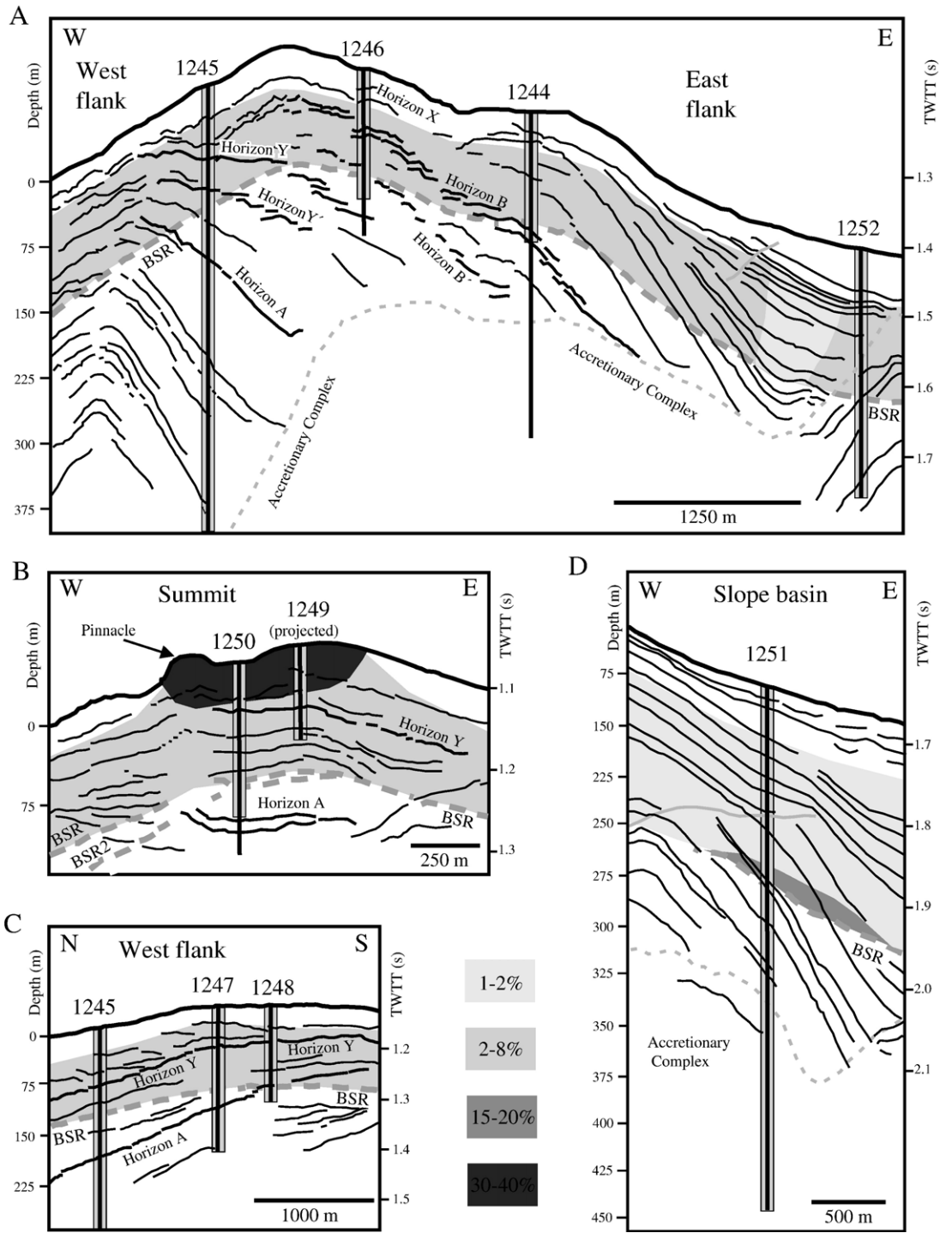


Fig. 2. Line-drawings of multi-channel seismic profiles (Tréhu et al., 2004a) across different portions of southern Hydrate Ridge. A) W–E section across the northern part of southern Hydrate Ridge. B) W–E section across the summit of southern Hydrate Ridge. C) N–S section along the west flank of southern Hydrate Ridge. D) W–E section across the lowermost part of the slope basin east of Hydrate Ridge. The bottom simulating reflector (BSR), main seismic horizons, and ODP Leg 204 drill sites are indicated. Grey shading indicates average gas hydrate concentrations (as % of pore space) estimated by Tréhu et al. (2004a). Data presented here correspond to the stratigraphic intervals marked by the grey shaded box at each site.

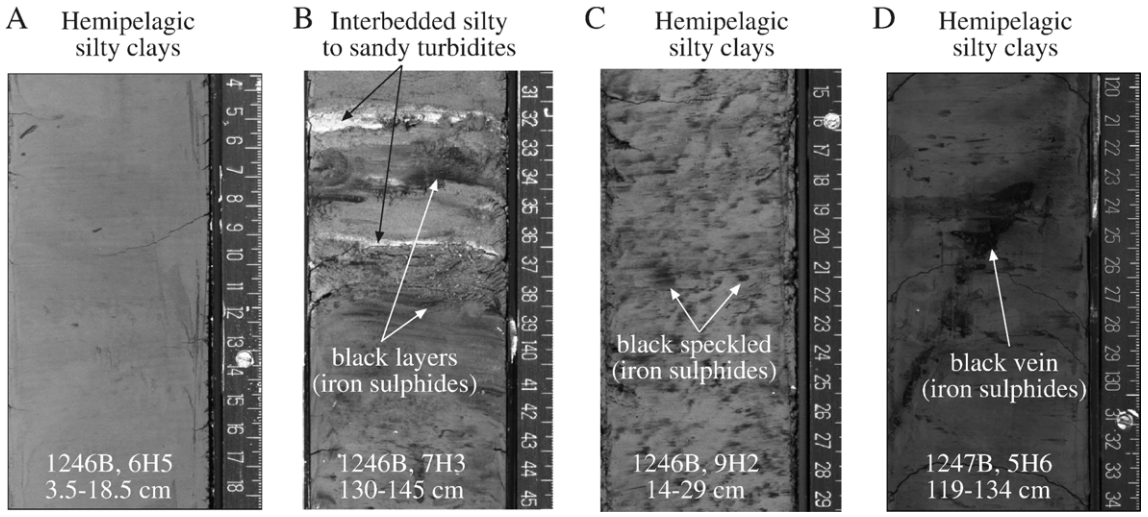


Fig. 3. Core images of representative sediment types identified during ODP Leg 204 and diagenetic features involving iron sulphides.

a sample using a high magnetic field normalized by its low-field magnetic susceptibility ($\chi$) has been used as a first-order indicator for the presence of greigite (Snowball, 1991; Roberts, 1995; Frank et al., 2007) and pyrrhotite (Housen and Musgrave, 1996). This parameter offers the possibility to screen large sample sets (including u-channel samples) for the presence of magnetic iron sulphides.

Our approach has been to: 1) determine the IRM/$\chi$ ratio for a large set of samples; and 2) identify magnetic iron sulphides, using thermal demagnetization of composite IRMs, hysteresis experiments, FORC analyses and SEM observations, in a sub-set of representative samples with variable IRM/$\chi$ ratios. The IRM/$\chi$ ratio was determined for 549 sediment samples collected during ODP Leg 204 on board the *RV Joides Resolution* using 8-cm$^3$ plastic cubes. These samples were taken at 10-m stratigraphic intervals, except in selected intervals such as in the vicinity of gas hydrates, where sampling was increased to 1.5 m intervals. Twelve additional samples were taken nearby gas hydrates from sediment cores stored in liquid nitrogen at the Research Centre for Ocean Margins of the University of Bremen, Germany. IRM/$\chi$ ratios were measured at the Paleomagnetic Laboratory (UB-CSIC) of the Institute of Earth Sciences *Jaume Almera* in Barcelona, Spain. $\chi$ was measured with a KLY-2 magnetic susceptibility bridge using a field of 0.1 mT at a frequency of 470 Hz. An IRM was produced using a Molspin pulse magnetizer with a field of 0.9 T (IRM@0.9 T). The IRM@0.9 T was measured using a 2G Enterprises three-axis cryogenic magnetometer. IRM@0.9 T is used to produce IRM/$\chi$ ratios, which are therefore referred to as IRM@0.9 T/$\chi$. IRM@0.9 T could not be measured for some samples because of strong magnetizations. All magnetic properties were normalized by the dry weight of the samples.

Identification of magnetic minerals was conducted by combining thermal demagnetization of composite IRMs, hysteresis measurements, FORC analysis, and SEM observations of 33 selected samples with a range of IRM@0.9 T/$\chi$ ratios. For 25 of these 8-cm$^3$ samples, a 1-cm$^3$ cube was sub-sampled using a ceramic knife. Hysteresis and FORC analyses were conducted on the 1-cm$^3$ cubes using a Princeton Measurements Corporation Micromag 2900 vibrating sample magnetometer (VSM) at the National Oceanography Centre, Southampton (NOCS), UK. Hysteresis loops were measured using a maximum field of 1 T and magnetic parameters were determined after paramagnetic slope correction of the loop. The measured hysteresis parameters include saturation magnetization ($M_s$), saturation remanence ($M_{rs}$), coercive force ($B_c$), and the coercivity of remanence ($B_{cr}$), which was measured by progressive backfield demagnetization of the IRM imparted at 1 T. The same 1-cm$^3$ cubes were used to obtain resin-impregnated polished sections perpendicular to the bedding plane. These sections were examined at the NOCS using a LEO 1450VP SEM operated at 20 keV. Elemental analyses were obtained using a Princeton Gamma Tech (IMIX-PTS) energy dispersive spectrometer (EDS) with a 2–3 μm diameter X-ray beam. A pyrite standard was used to calibrate analyses of iron sulphide minerals. For the 8 remaining samples, a composite IRM applied at fields of 0.9, 0.3 and 0.1 T along the three mutually perpendicular sample axes was thermally demagnetized using a Schonstedt furnace and measured in an air

atmosphere using the 2G magnetometer at the UB-CSIC laboratory.

## 4. Results

### 4.1. IRM@0.9 T/χ ratios

Samples fall into one of three groups according to their IRM@0.9 T/χ and χ values (Fig. 4A) (see Supplementary data, Table 2). The first group (labelled as Type 1) is characterized by low IRM@0.9 T/χ (<15 kA/m) and low χ (<$3\times10^{-7}$ $m^3$/kg) values. The second group (Type 2) is characterized by similarly low IRM@0.9 T/χ and higher χ (up to $1.7\times10^{-6}$ $m^3$/kg) values. The third group (Type 3) is characterized by high IRM@0.9 T/χ values (between 15 and 100 kA/m) and χ values slightly higher than those of Type 1 samples (between 1.5 and $6\times10^{-7}$ $m^3$/kg). Type 1 samples are the most abundant (~70–75%) and correspond to the hemipelagic clays and silty clays that predominate in SHR sediments. Type 2 samples are scarce (<2%), and correspond to turbidite layers. Type 3 samples (~20–25%) correspond to hemipelagic clays and silty clays that, in many cases, contain the millimetre- to centimetre-scale iron sulphide nodules that produce the characteristic black speckled pattern within the sediments (Fig. 3C,D).

A recent compilation of mineral magnetic data of known magnetic minerals (Peters and Dekkers, 2003)

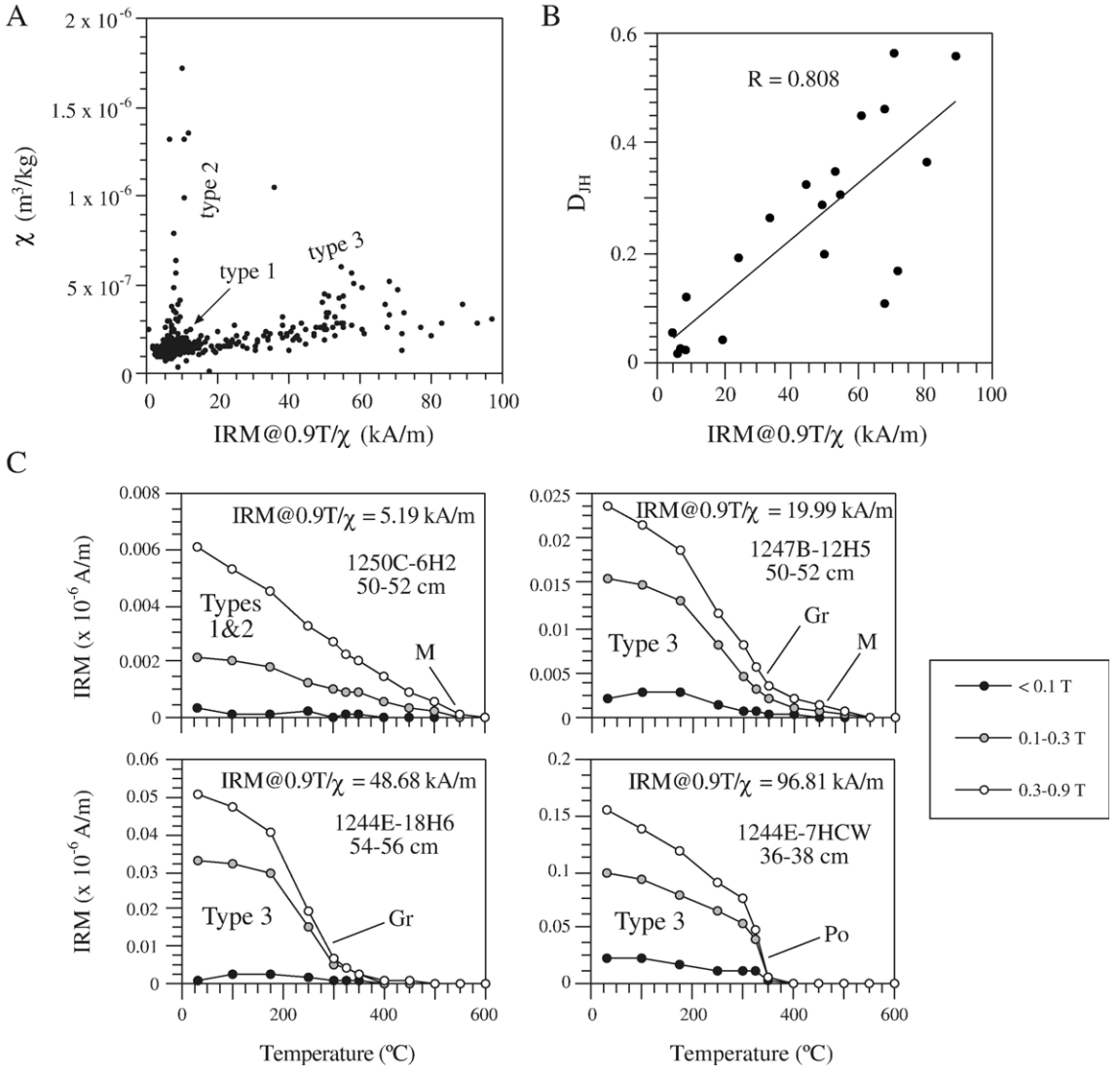


Fig. 4. A) Plot of IRM@0.9 T/χ against χ data for all studied samples. B) Comparison of IRM@0.9 T/χ with $D_{JH}$. C) Thermal demagnetization results of representative samples with increasing IRM@0.9 T/χ ratios. Gr: greigite; Po: pyrrhotite; M: magnetite.

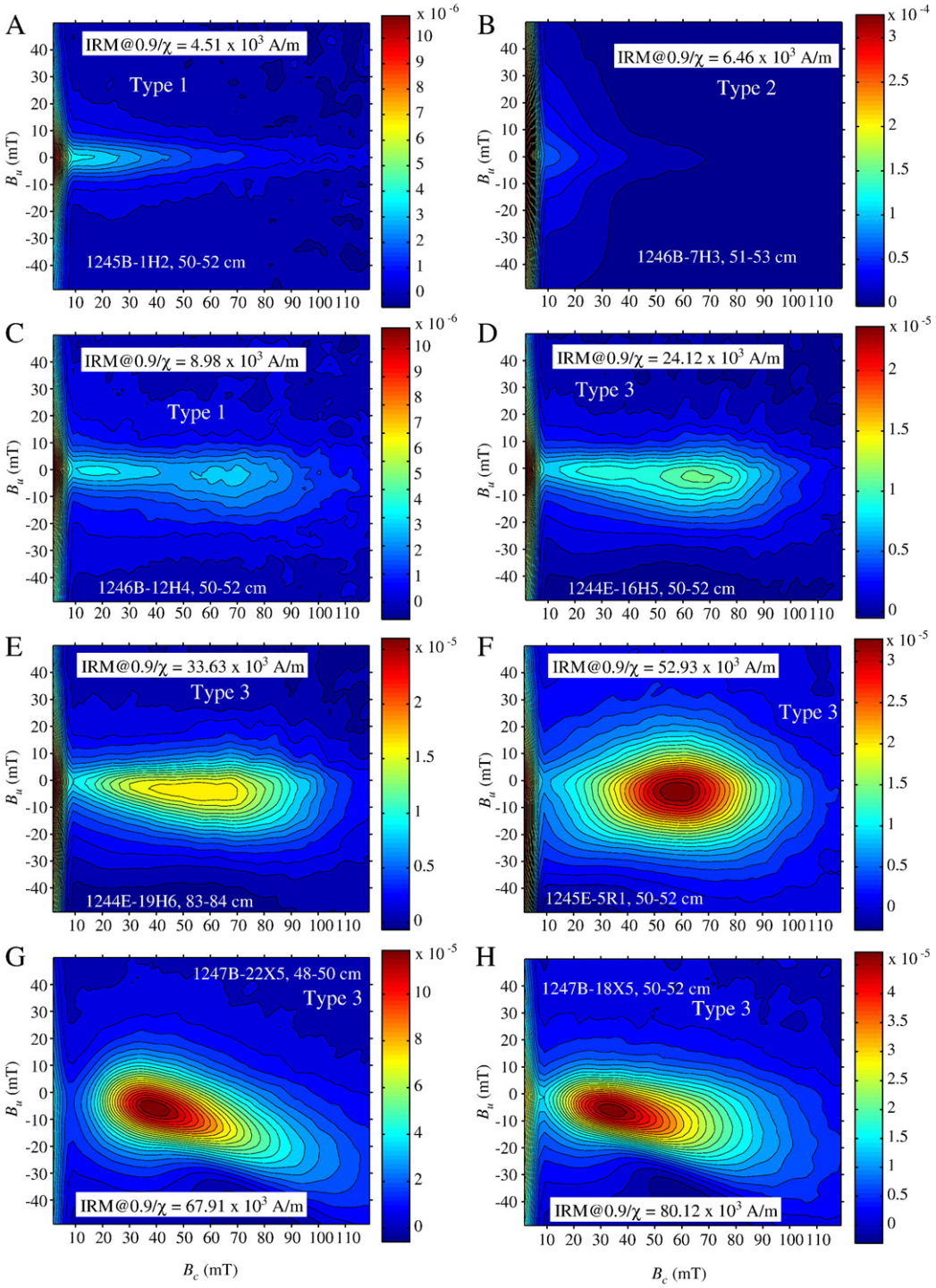


Fig. 5. FORC distributions for representative samples with increasing IRM@0.9 T/χ ratios. An averaging time of 250 ms was used for all measurements and a smoothing factor of 5 was used to construct the FORC diagrams (see Roberts et al., 2000 for explanation). Colour scale represents magnetic moment (in $Am^2$).

provides a first-order interpretation of IRM@0.9 T/χ ratios. According to this compilation, and in the absence of iron (hydr)oxides such as hematite and goethite in the SHR sediments (Housen and Musgrave, 1996; Musgrave et al., 2006; Larrasoaña et al., 2006), IRM@0.9 T/χ ratios of up to 15 kA/m (Type 1 and 2 samples) might be

diagnostic of magnetite-dominated assemblages. Intermediate IRM@0.9 T/$\chi$ values between 15 and 60 kA/m (Type 3 samples) are likely to indicate mixtures of magnetite and variable amounts of greigite, and even higher IRM@0.9 T/$\chi$ values (>60 kA/m) in some Type 3 samples might indicate the presence of pyrrhotite.

### 4.2. Magnetic mineralogy and significance of IRM@0.9 T/$\chi$ ratios

Hysteresis results, in the form of the $D_{JH}$ parameter (Housen and Musgrave, 1996; Musgrave et al., 2006), correlate well with IRM@0.9 T/$\chi$ values (Fig. 4B). $D_{JH}$ is obtained by normalizing $M_r/M_{rs}$ by the $B_{cr}/B_c$ ratio, and is >0.33 for SD and <0.01 for MD particles, respectively. Many natural magnetic iron sulphide samples have SD properties (Roberts, 1995; Roberts et al., 2006), therefore the highest $D_{JH}$ values point to the predominance of magnetic iron sulphides in samples with the largest IRM@0.9 T/$\chi$ ratios.

Thermal demagnetization of a three-component IRM (Fig. 4C) provides initial validation of the interpretation based on IRM@0.9 T/$\chi$ results. Type 1 and 2 samples are characterized by a steady decrease in the intensity of the three IRM components, which disappear completely below 600 °C, and therefore indicates the predominance of magnetite. Type 3 samples have a different demagnetization pattern. IRM intensities of samples with IRM@0.9 T/$\chi$ <60 kA/m undergo a sharp decrease between 200 °C and 300 °C, which is typical of greigite (Roberts, 1995). IRM intensities of samples with IRM@0.9 T/$\chi$ >60 kA/m undergo a sharp decrease above 300 °C, which is better explained by pyrrhotite (Dekkers, 1989).

FORC distributions for most Type 1 samples are characterized by a peak near 20 mT, which has elongated contours toward higher coercivities (Fig. 5A). These results are consistent with the presence of coarse SD and PSD magnetite grains in Type 1 samples. FORC distributions of Type 2 samples are characterized by a contour pattern that diverges away from the origin of the plot (Fig. 5B), which can be attributed to MD magnetite particles (Roberts et al., 2000). The apparent increase in magnetite grain size found in Type 2 compared to Type 1 samples can be attributed to the textural difference between hemipelagic sediments and turbidites. For some Type 1 samples with higher (~10 kA/m) IRM@0.9 T/$\chi$ ratios, a second peak in the FORC distribution is observed at 60–70 mT. This peak is similar in intensity to that found at 20 mT, and can be attributed to greigite (Roberts et al., 2000; Rowan and Roberts, 2006; Roberts et al., 2006) (Fig. 5C). In Type 3 samples with increasing IRM@0.9T/$\chi$ ratios of up to 60 kA/m, the intensity of this peak progressively increases, and so does its vertical spread and offset below the $B_u$=0 axis (Fig. 5D–F). This change in the FORC distribution with increasing IRM@0.9 T/$\chi$ ratios can be interpreted as being due to the increasing abundance of strongly interacting SD greigite particles (Roberts et al., 2000, 2006), which progressively overwhelm the contribution of magnetite. FORC distributions of Type 3 samples with IRM@0.9 T/$\chi$ ratios higher than 60 kA/m are characterized by a peak centred at 40 mT (Fig. 5G,H), with a prominent "kidney" shape toward higher coercivities. Similar FORC distributions have been reported for pyrrhotite-bearing sediments (Weaver et al., 2002; Wehland et al., 2005; Roberts et al., 2006).

Conclusive identification of magnetic minerals from the SHR sediments is provided by SEM images and EDS results from representative samples with variable IRM@0.9 T/$\chi$ ratios (Fig. 6). Most of the samples, regardless of their type, contain framboidal and euhedral pyrite. Moreover, large magnetite grains with variable Ti contents, which are best represented in Type 2 (turbidite) samples, are found in most of the studied samples (Fig. 6a). Neither greigite nor pyrrhotite have been found in samples with IRM@0.9 T/$\chi$ <15 kA/m (Types 1 and 2). The most significant feature found in Type 1 samples is the occasional occurrence of millimetre-scale siderite cemented nodules that have discontinuously grown over pyrite and other sediment components such as quartz (Fig. 6b). Another significant feature, regardless of sample type, is the occasional presence of sub-millimetre to centimetre-scale gypsum nodules (Fig. 6e). Type 3 samples with IRM@0.9 T/$\chi$ between 15 and 60 kA/m contain variable amounts of fine-grained greigite. Greigite is found growing either within cleavages of sheet silicate grains or around pyrite aggregates (Fig. 6c). In the later case, greigite has overgrown at least two different generations of pyrite that are found either within microenvironments associated with foraminifera shells (Fig. 6c) or that are dispersed in the sediment matrix (Fig. 6e). The first generation of pyrite (Py1) is constituted by framboids that often have euhedral overgrowths (Fig. 6c), and the second generation (Py2) is constituted by dispersed grains that have grown over previously formed framboids. Pyrrhotite is found only in Type 3 samples with IRM@0.9 T/$\chi$ >60 kA/m (Fig. 6d–f). Pyrrhotite occurs in sub-millimetre to centimetre size nodules that are invariably associated with siderite. These nodules comprise aggregates of individual platy pyrrhotite grains that usually range between 20 and 30 μm in

size. These grains grew either within or around patches of siderite cement, which, in turn, grew over quartz, pyrite and other sediment components such as corroded bioclasts (Fig. 6f). X-ray energy dispersive spectra of individual pyrrhotite grains give a mean Fe/S ratio of 46.1±0.5/53.9±0.5, which is entirely consistent with the $Fe_7S_8$ composition of monoclinic (ferrimagnetic) pyrrhotite.

The combination of hysteresis data, thermal demagnetization of composite IRMs, FORC diagrams and SEM images provides compelling evidence for a link between specific magnetic mineral assemblages and

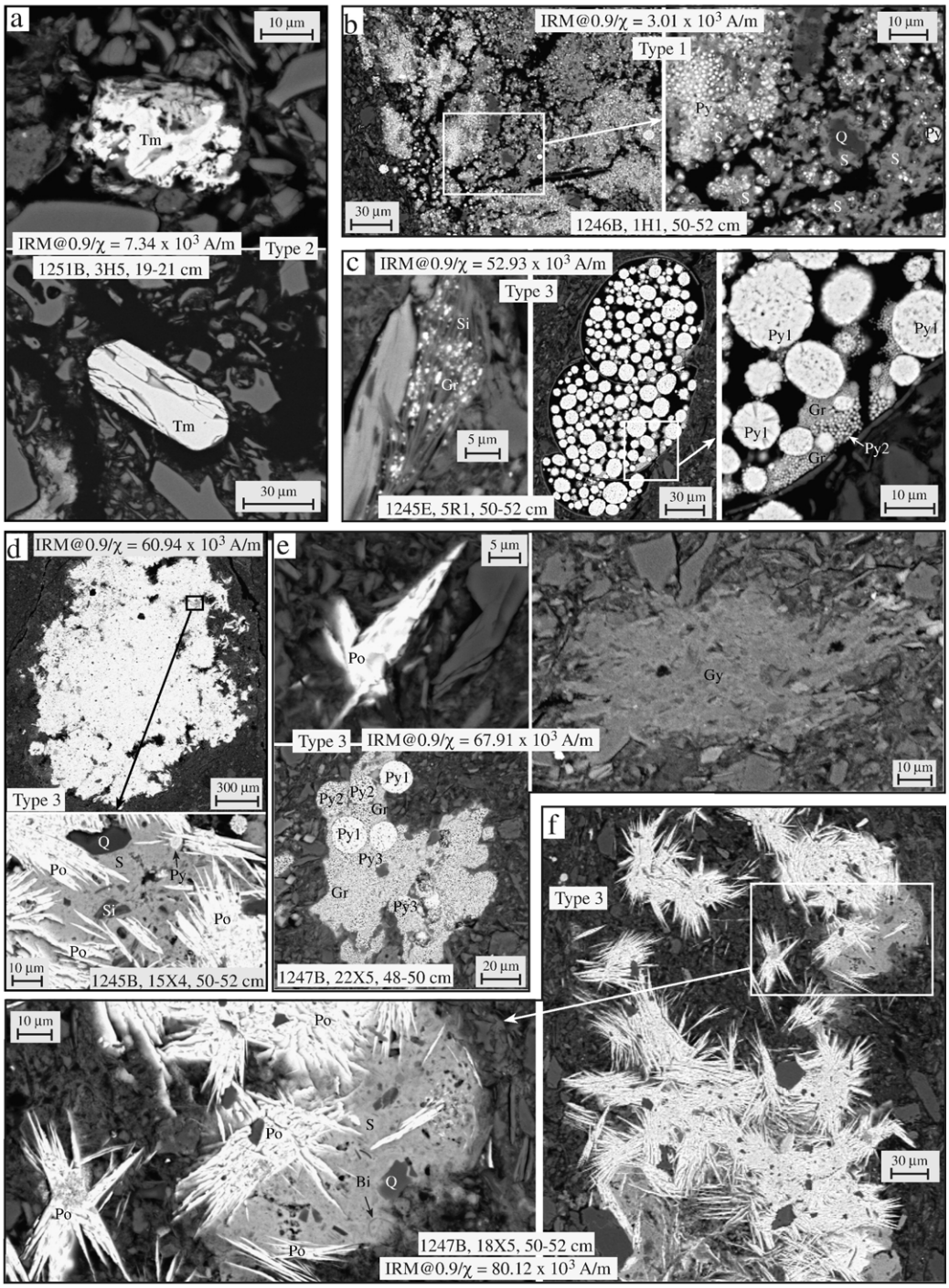

IRM@0.9 T/$\chi$ ratios in the studied SHR sediments. Type 1 and 2 samples, which are characterized by low IRM@0.9 T/$\chi$ ratios (<15 kA/m), are dominated by magnetite (Figs. 4C, 5A,B and 6a). Samples with IRM@0.9 T/$\chi$ between 15 and 30 kA/m (referred to as Type 3a) are characterized by mixtures of similar amounts of magnetite and greigite (Figs. 4C, 5D). IRM@0.9 T/$\chi$ ratios between 30 and 60 kA/m (Type 3B) are indicative of magnetic assemblages that are dominated by greigite (Figs. 4C, 5E,F and 6c). Moreover, samples with IRM@0.9 T/$\chi$ >60 kA/m (Type 3c) are dominated by pyrrhotite (Figs. 4C, 5G,H and 6d–f), although they often also contain greigite (e.g. Fig. 6e). Thermal demagnetization results indicate that, despite the occurrence of some Ti-rich magnetite grains, their contribution to the bulk magnetic properties appears to be negligible since no systematic IRM intensity decay attributable to their occurrence is observed in any of the studied samples (Fig. 4C).

## 5. Discussion

Diagenetic reactions in marine sediments are mainly driven by the metabolic activity of microbes, which use a sequence of progressively less-efficient oxidants to degrade buried organic matter (Froelich et al., 1979; Roberts and Weaver, 2005). This sequence involves consumption of oxygen (under oxic conditions), nitrate, manganese and iron oxides (under sub-oxic conditions), and sulphate and carbon dioxide (under anoxic conditions), until organic matter is eventually exhausted. Microbially-mediated reduction of sulphate during earliest diagenesis releases sulphide, which reacts with iron-bearing minerals and dissolved iron to form pyrite. When sulphate is exhausted during burial, at depths below the sulphate zone, reduction of carbon dioxide results in formation of methane (Froelich et al., 1979; Roberts and Weaver, 2005). Under these conditions, dissolved iron can react with other ions to form other authigenic minerals, such as siderite ($FeCO_3$) if pore waters become saturated with respect to this carbonate. If the dissolved methane reaches saturation, gas hydrate will form. Methane can also migrate upward until it enters the sulphate zone, where it is anaerobically oxidized. This process, which is mediated by consortia of sulphate-reducing bacteria and methanotrophic archaea (Boetius et al., 2000), releases sulphide, which will react with any surviving iron-bearing mineral or dissolved iron to form iron sulphides (Froelich et al., 1979; Riedinger et al., 2005; Roberts and Weaver, 2005).

### 5.1. Diagenetic environments and origin of greigite and pyrrhotite in SHR sediments

The three diagenetic settings where sedimentary magnetic iron sulphides have been claimed to form, e.g. sulphate zone, zone of anaerobic oxidation of methane (AOM), and zone of methanogenesis and gas hydrate formation, are presently active at SHR because organic carbon contents of SHR sediments, which vary between 0.9 and 1.6 (wt.%), are high enough to sustain sulphate reduction in the sulphate and AOM zones and to enable methanogenesis and gas hydrate formation in underlying sediments (Claypool et al., 2006). To determine whether these processes represent significant factories for diagenetic greigite and pyrrhotite, we evaluate the diagenetic pathway of the SHR sediments, and the concomitant changes in their magnetic mineralogy, in light of the geochemical framework described above.

#### 5.1.1. Sulphate zone

The sulphate zone, where sulphate is mainly reduced during bacterial degradation of organic matter, is found at depths <9 mbsf at sites 1244–1247, 1251 and 1252 (Borowski, 2006; Torres and Rugh, 2006; Claypool et al., 2006) (Fig. 7A). All samples located within this zone are characterized by IRM@0.9 T/$\chi$ <15 kA/m, which indicates the predominance of magnetite. Incipient formation of greigite might occur at about 2–4 mbsf in Site 1252 according to observed IRM@0.9 T/$\chi$ values near 15 kA/m. IRM@0.9 T/$\chi$ data are sparse, so magnetic susceptibility variations provide a higher resolution data set from which to infer mineral magnetic variations. The most conspicuous pattern in the sulphate zone is the loss of magnetic susceptibility from a peak value of 30–50 ($\times 10^{-7}$ SI) near the sediment–water interface to a background value of ~20 ($\times 10^{-7}$ SI) just

Fig. 6. Back-scattered scanning electron microscope images of selected samples with increasing IRM@0.9 T/$\chi$ ratios. a) Examples of titanomagnetite grains with variable Ti contents (Tm), of probable detrital (dissolved edges, upper grain) and volcanic (lower grain) origin. b) Nodule formed by overgrowth of siderite (S) over pyrite (Py), quartz (Q) and other sediment constituents. c) Sample containing greigite (Gr) that grows between the cleavage planes of an iron-bearing detrital sheet silicate (Si) and around recrystallized pyrite framboids (Py1) and space-filling pyrite grains (Py2). d) Nodule formed by pyrrhotite (Po) plates that have overgrown a siderite (S) cement containing framboidal pyrite (Py), quartz (Q) and iron-bearing detrital sheet silicates (Si). e) Sample containing gypsum nodules (Gy), pyrrhotite plates (Po), and greigite (Gr) growing around recrystallized (Py1) and non-recrystallized (Py2) pyrite framboids, and around space-filling pyrite grains (Py3). f) Nodule formed by pyrrhotite (Po) plates that overgrow a siderite (S) cement containing quartz (Q), replaced bioclastic grains (Bi), and other sediment constituents.

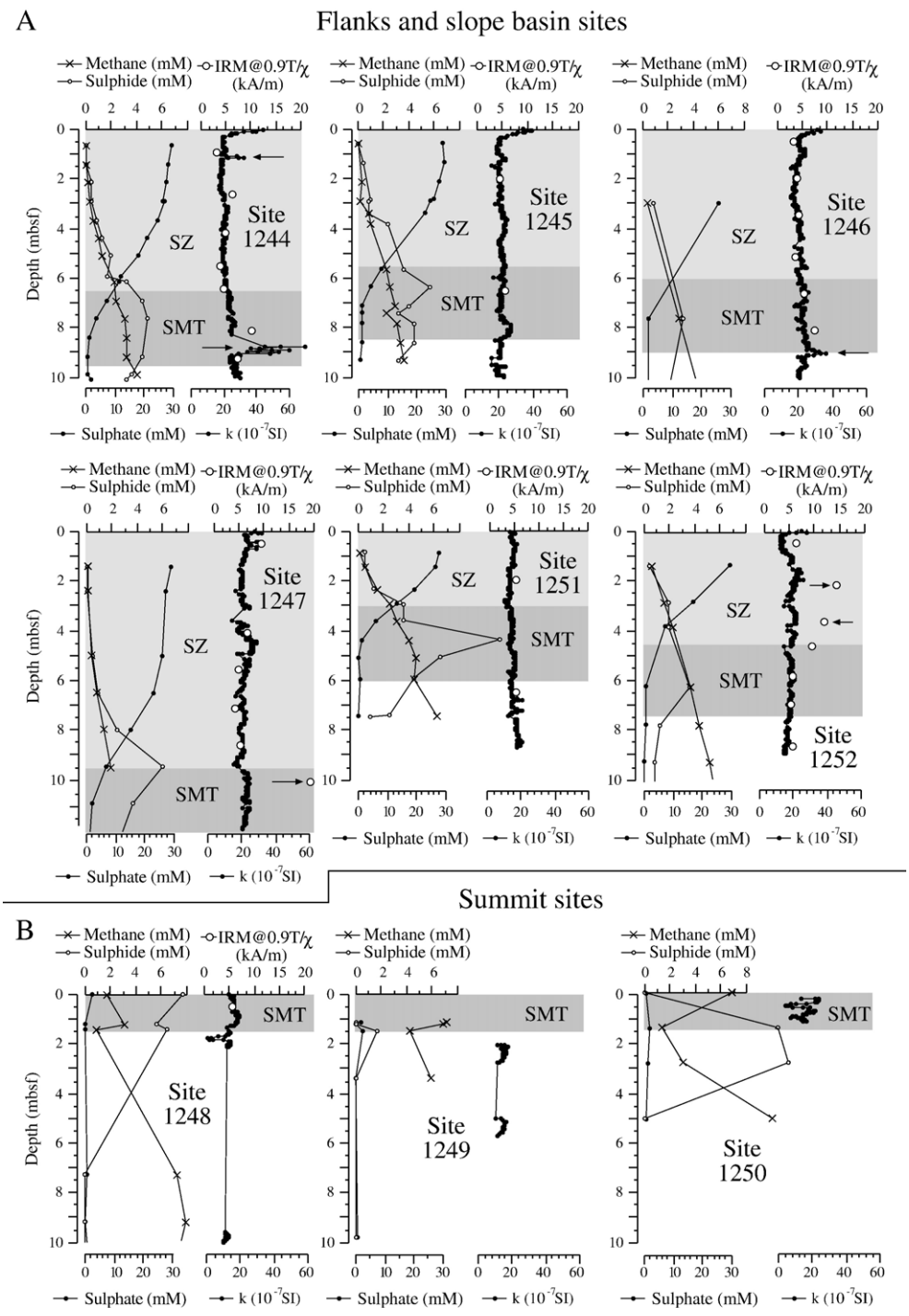


Fig. 7. Depth variations of IRM@0.9 T/$\chi$, shipboard measurements of volume magnetic susceptibility ($k$) (Tréhu et al., 2003), and pore-water sulphide, sulphate (Borowski, 2006) and methane (Tréhu et al., 2003) concentrations for sites located (A) on the flanks and slope basin, and (B) on the summit of SHR. The position of the sulphate zone (SZ) and the sulphate–methane transition (SMT) is based on geochemical data reported by Tréhu et al. (2003). Arrows indicate possible occurrences of greigite as derived from IRM@0.9 T/$\chi$ data and magnetic susceptibility logs.

20–30 cm underneath. This pattern probably reflects reductive dissolution of magnetite grains during earliest diagenesis. The shallowest discrete samples were collected 50–52 cm below the seafloor, so the magnetic properties of Type 1 and 2 samples reflect the presence of relatively coarser magnetite grains that survived

reductive dissolution during earliest diagenesis and that, most likely, constitute the background magnetic assemblage present after earliest diagenetic reactions. A peak in magnetic susceptibility (~40 ($\times 10^{-7}$ SI) is observed at ~1 mbsf in Site 1244. This peak does not correspond to any turbidite bed, and might therefore be interpreted as due to the occurrence of greigite. Formation and preservation of greigite in the sulphate zone requires limited production of sulphide as a result of sulphate reduction, which prevents completion of pyritization reactions (Liu et al., 2004). High accumulation rates in sediments within the sulphate zone, which reach up to 70 cm/kyr at SHR (Tréhu et al., 2003) and which dilute organic carbon burial and therefore limit sulphide production, probably explains the occurrence of greigite in shallow sediments at some intervals.

*5.1.2. AOM zone*

The AOM zone is considered here as approximately coincident with the sulphate methane transition (SMT), where upward diffusing methane and downward diffusing sulphate are stoichiometrically consumed in the AOM process. The AOM zone is found at the sediment–water interface in the summit sites (sites 1248–1250), where upward flux of methane and rates of AOM are highest, and at variable depths between 3 and 11.5 mbsf in flank and slope basin sites (sites 1244–1247, 1251 and 1252), where upward methane fluxes and rates of AOM are considerably lower (Borowski, 2006; Torres and Rugh, 2006; Claypool et al., 2006). IRM@0.9 T/$\chi$ and magnetic susceptibility data point to the occurrence of greigite in some horizons at sites 1244, 1246 and 1247 located just 0.5 to 1.5 m underneath maxima in dissolved sulphide concentrations (Fig. 7A). In the summit sites, the IRM@0.9 T/$\chi$ value of the only discrete sample available (<6 kA/m) indicates the predominance of magnetite (Fig. 7B). For the thin stratigraphic intervals where magnetic susceptibility data are available, its values are lower than, or near, background values of 20 ($\times 10^{-7}$ SI). This suggests that reductive diagenesis of magnetite starts at the sediment–water interface, and also that greigite did not form in the shallowest sediments, at the summit sites. The main factor controlling formation of greigite in the AOM zone is the interplay between the rates of downward sulphate and upward methane diffusion, which in turn controls the amount of sulphide produced (Kasten et al., 1998; Neretin et al., 2004; Jørgensen et al., 2004). High availability of methane in sediments from the summit of the SHR probably allowed production of large amounts of sulphide, which will have prevented greigite preservation by enabling pyritization reactions to be fully completed, as is the case in other settings (Passier et al., 1998; Garming et al., 2005; Riedinger et al., 2005). In the flank and slope basin sites, lower methane fluxes will have allowed less sulphide formation, which might have enabled preservation of greigite. This scenario has been documented at other localities (Kasten et al., 1998; Neretin et al., 2004; Jørgensen et al., 2004).

*5.1.3. Methanic and gas hydrate zone*

We have examined the link between magnetic iron sulphides and gas hydrates by considering the magnetic properties of discrete sediment samples located within the GHSZ in the vicinity of gas hydrates, as follows: 1) sediments located adjacent to massive gas hydrate accumulations which were stored in liquid nitrogen (12 samples); 2) sediments with soupy textures, which are related to dissociation of massive gas hydrate accumulations (Tréhu et al., 2003) (5 samples); 3) sediments located within infra-red detected temperature anomalies (Weinberger et al., 2005), which are mostly related to massive accumulations of gas hydrates (15 samples); 4) sediments with mousse-like textures, which are related to dissociation of disseminated gas hydrates (Tréhu et al., 2003) (9 samples); and 5) sediments located outside of, but <50 cm away from, temperature anomalies (Weinberger et al., 2005) (58 samples). Overall, the first three types of samples correspond to sediments located in the vicinity of massive gas hydrate accumulations, whereas the last two types correspond to sediments located near disseminated gas hydrates. Samples related to massive gas hydrate deposits contain, at most, small proportions of greigite (Fig. 8A). On the contrary, samples related to disseminated gas hydrate deposits often contain larger amounts of greigite, and also pyrrhotite (Fig. 8A). These findings therefore suggest that the occurrence of greigite and pyrrhotite is favoured by high concentrations of methane, which might be sufficient to enable formation of disseminated gas hydrates but not to enable massive gas hydrate accumulations. This interpretation is supported by the occurrence of nodules composed of magnetic iron sulphides along high-angle fractures, which act as conduits for migration of methane (Tréhu et al., 2003) but which do not contain gas hydrates (Fig. 3D). The apparent link between the occurrence of magnetic iron sulphides and gas hydrates suggests that greigite and pyrrhotite are being produced at those locations, throughout the GHSZ, where gas hydrates are now present. We are unaware of any published specific mechanism that might explain the formation of greigite and pyrrhotite well below the AOM zone. Before proposing a mechanism, we need first to examine microtextural relationships between greigite and pyrrhotite and other sediment constituents.

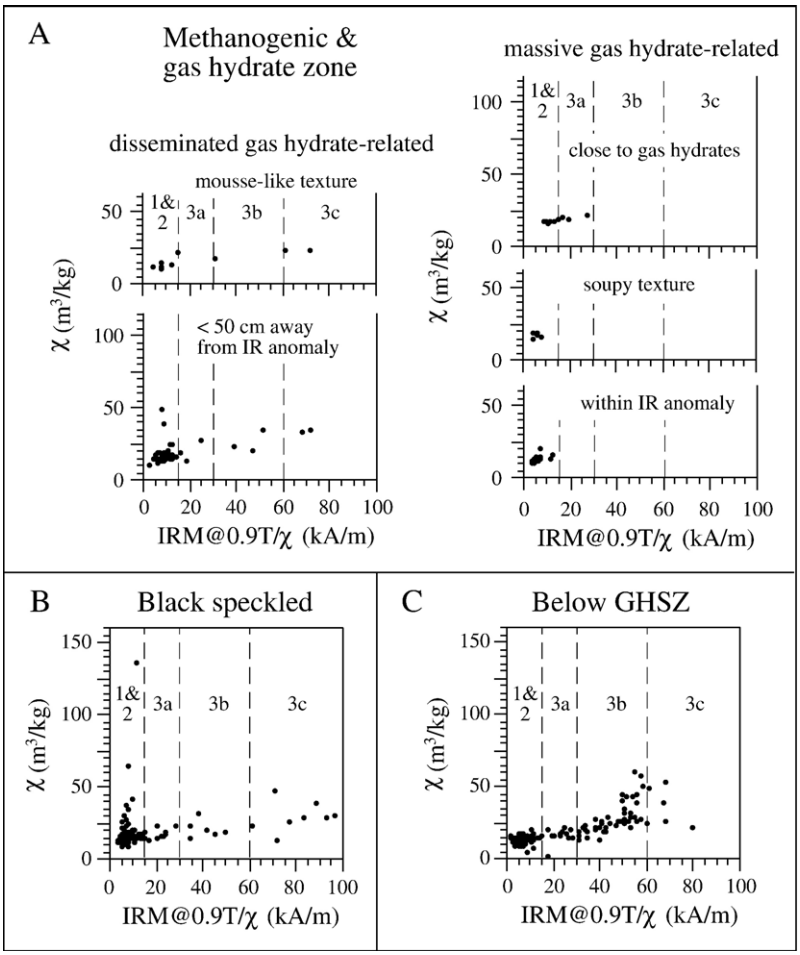


Fig. 8. A) Plot of IRM@0.9 T/χ against χ for samples related to massive and disseminated gas hydrates. B) Samples from within the GHSZ that display the characteristic black speckled pattern and that are not included in the present-day sulphate and AOM zone or in the vicinity of gas hydrates. C) Samples located below the GHSZ. The dashed lines mark the fields for IRM@0.9 T/χ ratios lower than 15 kA/m (magnetite-dominated samples; Types 1 and 2), between 15 and 30 kA/m (mixtures of magnetite and greigite; Type 3a samples), between 30 and 60 kA/m (greigite-dominated samples, Type 3b), and larger than 60 kA/m (pyrrhotite-bearing samples; Type 3c).

### *5.2. Timing and significance of greigite and pyrrhotite formation*

Authigenic greigite and pyrrhotite in deep sediments from the SHR always grew over iron-bearing minerals, but not over all sulphur-bearing minerals (Fig. 6). This indicates that formation of greigite and pyrrhotite results from the interaction of dissolved sulphide with highly reactive (towards sulphide) iron on the surface of iron-bearing minerals. In the sulphate and AOM zones, greigite is the only magnetic iron sulphide present. SEM observations demonstrate that greigite often grew within aggregates composed of at least two different generations of pyrite (Fig. 6c,e). These textures suggest that greigite grew after early diagenetic euhedral overgrowth of pyrite framboids under evolving pore water conditions (Raiswell, 1982). The textures described here for pyrite–greigite aggregates, which are similar to those reported elsewhere (Jiang et al., 2001; Roberts and Weaver, 2005; Rowan and Roberts, 2006), are consistent with formation related to the supply of sulphide in the sulphate and AOM zones. These diagenetic environments occur in shallow (<11 mbsf) sediments at SHR, and likely also in other methane-rich settings. Therefore, any greigite formed in the sulphate and AOM zones will probably record a remanence that will be delayed with respect to the depositional age of the host sediment. For accumulation rates of 30 cm/kyr that are typical for SHR (Tréhu et al., 2003), this would lead to an expected delay in remanence acquisition of a few (<40) thousand years.

Both greigite and pyrrhotite have been reported in the gas hydrate zone. SEM observations indicate that greigite has also grown on the surface of iron-bearing sheet silicates (Fig. 6c). Given the slow kinetics of sheet silicate dissolution, whose half-live of reaction with sulphide is of the order of hundreds of kyr (Canfield et al., 1992), this microtexture suggests that greigite has a late origin. Pyrrhotite occurs in sub-millimetre to centimetre-scale nodules that are invariably associated with siderite (Fig. 6d–f). Siderite is typically formed in non-sulphidic, methanic environments located below the sulphate and AOM zones (Froelich et al., 1979). However, siderite can also grow in shallow sediments within the sulphate zone, provided that the rate of iron reduction exceeds the rate of sulphate reduction and, therefore, that available sulphide does not consume all ferrous iron in solution (Pye et al., 1990). This explains the occurrence of siderite concretions not only within the deeper methanic zone (Fig. 6d,f), but also at shallow depths within the sulphate zone (Fig. 6b). Siderite nodules form through amalgamation of individual siderite nuclei, which results in preservation of residual porosity even after concretionary growth has terminated (Raiswell and Fisher, 2000). Pyrrhotite occurs as aggregates of individual platy grains either within or around patches of siderite cement (Fig. 6d–f). We interpret this texture to indicate the replacement of siderite by pyrrhotite, which grows not only on the outer surface of the siderite concretions, but also filling pore space within the nodules. The fact that pyrrhotite has grown in association with deep siderite cements that include corroded carbonate bioclasts (Fig. 6f), but not over siderite at shallow depths, strongly suggests that all pyrrhotite, as well as the greigite growing over sheet silicates, has a late origin within the methanic zone. Since the methanic and gas hydrate zone extends from the top of the methanic zone (>12 mbsf) to the base of the GHSZ (114–193 mbsf), any remanence carried by greigite and pyrrhotite formed in this setting is likely to record a remagnetization that will be significantly (and variably) delayed with respect to the depositional age of the host sediment. For accumulation rates of 30 cm/kyr that are typical for SHR (Tréhu et al., 2003), this would lead to delays ranging between a few (<40) thousand years and a few (<3) million years. This is consistent with observed remagnetizations associated with pyrrhotite nodules (Weaver et al., 2002) and with greigite that has grown over the surface of siderite nodules (Roberts and Weaver, 2005; Sagnotti et al., 2005).

Sulphate is depleted below 5–11 m at all sites, so a deep source of sulphide is required to form greigite and pyrrhotite within the methanic and gas hydrate zone at SHR. The interaction of saline marine and terrestrial fresh pore waters (Roberts and Weaver, 2005) and the injection of sulphate from underlying brines (Passier et al., 1998) can be excluded at SHR, therefore we suggest here another potential source of sulphide. Sulphate concentrations of pore waters are slightly increased at some locations in deep sediments from the SHR (Tréhu et al., 2003). Bottrell et al. (2000) suggested that such deep increases in sulphate concentration might result from anaerobic oxidation of pyrite, which might be driven by reduction of ferric iron released during diagenesis (Jiang et al., 2001) or of manganese oxides (Jørgensen and Nelson, 2004). Residual amounts of sulphate formed by this process might fuel deep AOM when they meet methane in the methanic and gas hydrate zone, in such a way that the resulting sulphide can diffuse and react with the surface of iron-bearing minerals to form greigite and pyrrhotite. This process provides a compelling mechanism to explain the occurrence of greigite and pyrrhotite in the methanic and gas hydrate zone. High concentration gradients of methane near massive gas hydrate layers are likely to exhaust deeply sourced sulphate, so that the rate of sulphide generation by deep AOM is large enough to drive pyritization reactions to completion. Smaller concentration gradients of methane near disseminated hydrates might lead to lower rates of sulphide generation by deep AOM, so that any greigite or pyrrhotite formed is not further converted into pyrite. Formation of greigite and pyrrhotite might be further stimulated by consortia of sulphate-reducing bacteria and methanotrophic archaea, whose activity is typically enhanced in the presence of dissolved methane and in the vicinity of disseminated gas hydrates, but not in the presence of massive gas hydrate accumulations (Wellsbury et al., 2000).

Only about one-third of the greigite- and pyrrhotite-bearing samples located within the GHSZ are found in the sulphate, the AOM, and the methanic and gas hydrate zones. Most of the rest of the greigite- and pyrrhotite-bearing samples within the GHSZ have the characteristic black speckled pattern (Figs. 3C, 8B). This pattern results from formation of pyrite and precursor iron sulphides such as mackinawite and/or greigite (Rickard and Morse, 2005), is typical of sediments undergoing sulphate reduction and AOM (Passier et al., 1998; Kasten et al., 1998; Neretin et al., 2004; Jørgensen et al., 2004; Garming et al., 2005; Rickard and Morse, 2005), and is common in samples located near disseminated gas hydrates at SHR. We therefore interpret the greigite and pyrrhotite in these black-speckled samples to have resulted from diagenetic reactions in the sulphate and AOM zones, and also in association

with methane and disseminated gas hydrates, during earlier stages of the sedimentary evolution of the SHR. Greigite and pyrrhotite that formed at much earlier times are also preserved in the sedimentary pile, as deduced from large IRM@0.9 T/$\chi$ values of many samples located well below (down to 520 mbsf) the base of the GHSZ (Fig. 8C), where active formation of magnetic iron sulphides is unlikely to occur.

## 6. Conclusions

Combined IRM@0.9 T/$\chi$ and hysteresis ratios, FORC, and SEM observations demonstrate the formation of authigenic greigite and pyrrhotite in different diagenetic environments within the GHSZ at SHR. Greigite is formed in shallow sediments (<12 mbsf) within the sulphate and AOM zones, and also in deep sediments (between 20 mbsf and the base of the GHSZ) within the methanic and gas hydrate zone. Pyrrhotite is found only in deep sediments. Geochemical conditions favourable for formation and preservation of greigite and pyrrhotite are a limited source of sulphide, whether it derives from microbially-driven sulphate reduction in the sulphate zone, in the AOM zone or in deep sediments, so that pyritization reactions are not driven to completion. Greigite and pyrrhotite in SHR sediments are invariably formed as a byproduct of the metabolism of microorganisms, so they can be considered as biologically induced minerals (Pósfai and Dunin-Borkowski, 2006).

Sulphate reduction, AOM, and formation/accumulation of methane are inherent to the diagenetic pathway undergone by gas hydrate-bearing marine sediments. Our results indicate that greigite and pyrrhotite are intimately associated with these three diagenetic environments, which suggests that diagenetic greigite and pyrrhotite might be used to detect ancient gas hydrate systems in the marine sedimentary record. Preservation of greigite and pyrrhotite appears to be prevented near high concentration gradients of methane in the vicinity of massive gas hydrate accumulations, whereas it is more abundant near low concentration gradients of methane near disseminated gas hydrates. These results indicate that rock magnetic identification of greigite and pyrrhotite should be useful for identifying ancient gas hydrate systems, because they can enable rapid screening of sedimentary sequences in the search for potential sediments that might have hosted methane and disseminated gas hydrates in the past. Moreover, formation of authigenic greigite and pyrrhotite at different depths implies that their magnetizations will have variable timings, which is likely to compromise paleomagnetic results of greigite- and pyrrhotite-bearing marine sediments.

## Acknowledgements

Samples were provided by the ODP, which is sponsored by the U.S. National Science Foundation and participating countries under management of Joint Oceanographic Institutions, Inc., in which Spain is included as part of the European Consortium for Ocean Research Drilling (ECORD). We are grateful for the use of the Paleomagnetic Laboratory of the SCT UB-CSIC. This research was supported by projects REN2001-5262-E, BTE2002-11698-E, REN2003-05996-MAR and CGL2006-12861-C02-02 (MEC, Spain). JCL benefits from a Ramón y Cajal contract (MEC) and EP from a FPU PhD fellowship (MEC). RJM acknowledges a Visiting Fellowship at the Institute for Rock Magnetism at the University of Minnesota. We thank Michael Winklhofer for providing the MATLAB code for processing the FORC diagrams shown in Fig. 5, and Gerhard Bohrmann for providing samples from frozen sediment cores. We thank Sabine Kasten and an anonymous reviewer, whose detailed and thoughtful comments greatly improved this manuscript, and Peggy Delaney, for editorial handling.

## Appendix A. Supplementary data

Supplementary data associated with this article can be found, in the online version, at doi:10.1016/j.epsl.2007.06.032.

## References

Boetius, A., Ravenschlag, K., Schubert, C.J., Rickert, D., Widdel, F., Gieseke, A., Amann, R., Jørgensen, B.B., Witte, U., Pfannkuche, O., 2000. A marine microbial consortium apparently mediating anaerobic oxidation of methane. Nature 407, 623–626.

Borowski, W.S., 2006. Data report: dissolved sulfide concentration and sulfur isotopic composition of sulfide and sulfate in pore waters, ODP Leg 204, Hydrate ridge and vicinity, Cascadia Margin, offshore Oregon. In: Tréhu, A.M., Bohrmann, G., Torres, M.E., Colwell, F.S. (Eds.), Proc. ODP, Sci. Res., vol. 204. Ocean Drilling Program, College Station, TX, pp. 1–13. doi:10.2973/odp.proc.sr.204.105.2006.

Bottrell, S.H., Parkes, R.J., Cragg, B.A., Raiswell, R., 2000. Isotopic evidence for anoxic pyrite oxidation and stimulation of bacterial sulphate reduction in marine sediments. J. Geol. Soc. Lond. 157, 711–714.

Canfield, D.E., Raiswell, R., Bottrell, S.H., 1992. The reactivity of sedimentary iron minerals toward sulfide. Am. J. Sci. 292, 659–683.

Claypool, G.E., Milkov, A.V., Lee, Y.J., Torres, M.E., Borowski, W.S., Tomaru, H., 2006. Microbial methane generation and gas transport in shallow sediments of an accretionary complex, southern Hydrate Ridge (ODP Leg 204), offshore Oregon, U.S.A. In: Tréhu, A.M., Bohrmann, G., Torres, M.E., Colwell, F.S. (Eds.), Proc. ODP, Sci. Res., vol. 204. Ocean Drilling Program, College Station, TX, pp. 1–52. doi:10.2973/odp.proc.sr.204.113.2006.

Cragg, B.A., Parkes, R.J., Fry, J.C., Weightman, A.J., Rochelle, P.A., Maxwell, J.R., 1996. Bacterial populations and processes in sediments containing gas hydrates (ODP Leg 146: Cascadia Margin). Earth Planet. Sci. Lett. 139, 497–507.

Dekkers, M.J., 1989. Magnetic properties of natural pyrrhotite. II. High- and low-temperature behaviour of $J_{rs}$ and TRM as a function of grain size. Phys. Earth Planet. Inter. 57, 266–283.

Dinarès-Turell, J., Dekkers, M.J., 1999. Diagenesis and remanence acquisition in the Lower Pliocene Trubi marls at Punta di Maiata (southern Sicily): paleomagnetic and rock magnetic observations. In: Tarling, D.H., Turner, P. (Eds.), Palaeomagnetism and diagenesis in sediments. The Geological Society, London, Spec. Publ., vol. 151, pp. 107–124.

Frank, U., Nowaczyk, N.R., Negendank, J.F.W., 2007. Rock magnetism of greigite bearing sediments from the Dead Sea, Israel. Geophys. J. Int. 168, 921–934.

Froelich, P.N., Klinkhammer, G.P., Bender, M.L., Luedtke, N.A., Heath, G.R., Cullen, D., Dauphin, P., Hammond, D., Hartman, B., Maynard, V., 1979. Early oxidation of organic matter in pelagic sediments of the eastern equatorial Atlantic: suboxic diagenesis. Geochim. Cosmochim. Acta 43, 1075–1090.

Garming, J.F.L., Bleil, U., Riedinger, N., 2005. Alteration of magnetic mineralogy at the sulfate–methane transition: analysis of sediments from the Argentine continental slope. Phys. Earth Planet. Inter. 151, 290–308.

Gràcia, E., Martínez-Ruiz, F., Piñero, E., Larrasoaña, J.C., Vizcaíno, A., Ercilla, G., 2006. Data report: grain-size, bulk and clay mineralogy of sediments from the summit and flanks of southern Hydrate Ridge (Sites 1244 to 1250), ODP Leg 204. In: Tréhu, A.M., Bohrmann, G., Torres, M.E., Colwell, F.S. (Eds.), Proc. ODP, Sci. Res., vol. 204. Ocean Drilling Program, College Station, TX, pp. 1–19. doi:10.2973/odp.proc.sr.204.110.2006.

Horng, C.S., Chen, K.H., 2006. Complicated magnetic mineral assemblages in marine sediments offshore southwestern Taiwan: possible influences of methane flux on the early diagenetic processes. Terr. Atmos. Oceanogr. Sci. 17, 1009–1026.

Horng, C.S., Roberts, A.P., 2006. Authigenic or detrital origin of pyrrhotite in sediments? Resolving a paleomagnetic conundrum. Earth Planet. Sci. Lett. 241, 750–762.

Horng, C.S., Torii, M., Shea, K.S., Kao, S.J., 1998. Inconsistent magnetic polarities between greigite- and pyrrhotite/magnetite-bearing marine sediments from the Tsailiao-chi section, southwestern Taiwan. Earth Planet. Sci. Lett. 164, 467–481.

Housen, B.A., Musgrave, R.J., 1996. Rock-magnetic signature of gas hydrates in accretionary prism sediments. Earth Planet. Sci. Lett. 139, 509–519.

Jiang, W.T., Horng, C.S., Roberts, A.P., Peacor, D.R., 2001. Contradictory magnetic polarities in sediments and variable timing of neoformation of authigenic greigite. Earth Planet. Sci. Lett. 193, 1–12.

Jørgensen, B.B., Nelson, D.C., 2004. Sulfide oxidation in marine sediments: geochemistry meets microbiology. In: Amend, J.P., Edwards, K.J., Lyons, T.W. (Eds.), Sulfur Biogeochemistry. Geol. Soc. Am. Special Paper, vol. 379. Geological Society of America, Boulder, Colorado, pp. 63–81.

Jørgensen, B.B., Böttcher, M.E., Lüschen, H., Neretin, L.N., Volkov, I.I., 2004. Anaerobic methane oxidation and a deep $H_2S$ sink generate isotopically heavy sulfides in Black Sea sediments. Geochim. Cosmochim. Acta 68, 2095–2118.

Kao, S.J., Horng, C.S., Roberts, A.P., Liu, K.K., 2004. Carbon–sulfur–iron relationships in sedimentary rocks from southwestern Taiwan: influence of geochemical environment on greigite and pyrrhotite formation. Chem. Geol. 203, 153–168.

Kasten, S., Freudenthal, T., Gingele, F.X., Schulz, H.D., 1998. Simultaneous formation of iron-rich layers at different redox boundaries in sediments of the Amazon deep-sea fan. Geochim. Cosmochim. Acta 62, 2253–2264.

Kvenvolden, K.A., 1993. Gas hydrates — geological perspective and global change. Rev. Geophys. 31, 173–187.

Larrasoaña, J.C., Gràcia, E., Garcés, M., Musgrave, R.J., Piñero, E., Martínez-Ruiz, F., Vega, M.E., 2006. Rock magnetic identification of magnetic iron sulfides and its bearings on the occurrence of gas hydrates, ODP Leg 204 (Hydrate Ridge). In: Tréhu, A.M., Bohrmann, G., Torres, M.E., Colwell, F.S. (Eds.), Proc. ODP, Sci. Res., vol. 204. Ocean Drilling Program, College Station, TX, pp. 1–33. doi:10.2973/odp.proc.sr.204.111.2006.

Liu, J., Zhu, R.X., Roberts, A.P., Li, S., Chang, J.H., 2004. High-resolution analysis of early diagenetic effects on magnetic minerals in post-middle-Holocene continental shelf sediments from the Korea Strait. J. Geophys. Res. 109, B03103. doi:10.1029/2003JB002813.

Lowrie, W., 1990. Identification of ferromagnetic minerals in a rock by coercivity and unblocking temperature properties. Geophys. Res. Lett. 17, 159–162.

Musgrave, R.J., Bangs, N.K., Larrasoaña, J.C., Gràcia, E., Hollamby, J.A., Vega, M.E., 2006. Rise of the base of the gas hydrate zone since the last glacial recorded by rock magnetism. Geology 34, 117–120.

Neretin, L.N., Böttcher, M.E., Jørgensen, B.B., Volkov, I.I., Lüschen, H., Hilgenfeldt, K., 2004. Pyritization processes and greigite formation in the advancing sulfidization front in the Upper Pleistocene sediments of the Black Sea. Geochim. Cosmochim. Acta 68, 2081–2093.

Passier, H.F., Dekkers, M.J., de Lange, G.J., 1998. Sediment chemistry and magnetic properties in an anomalously reducing core from the eastern Mediterranean Sea. Chem. Geol. 152, 287–306.

Peters, C., Dekkers, M.J., 2003. Selected room temperature magnetic parameters as a function of mineralogy, concentration and grain size. Phys. Chem. Earth 28, 659–667.

Pósfai, M., Dunin-Borkowski, R.E., 2006. Sulfides in biosystems. In: Vaughan, D.J. (Ed.), Reviews in Mineralogy and Geochemistry. Mineralogical Society of America, vol. 61, pp. 679–714.

Pye, K., Dickson, J.A.D., Schiavon, N., Coleman, M.L., Cox, M., 1990. Formation of siderite-Mg-calcite-iron sulphide concretions in intertidal marsh and sandflat sediments, north Norfolk, England. Sedimentology 37, 325–343.

Raiswell, R., 1982. Pyrite texture, isotopic composition and the availability of iron. Am. J. Sci. 282, 1244–1263.

Raiswell, R., Fisher, Q.J., 2000. Mudrock-hosted carbonate concretions: a review of growth mechanisms and their influence on chemical and isotopic composition. J. Geol. Soc. Lond. 157, 239–251.

Reynolds, R.L., Tuttle, M.L., Rice, C.A., Fishman, N.S., Karachewski, J.A., Sherman, D.M., 1994. Magnetization and geochemistry of greigite-bearing Cretaceous strata, North Slope basin, Alaska. Am. J. Sci. 294, 485–528.

Rickard, D., Morse, J.W., 2005. Acid volatile sulfide (AVS). Mar. Chem. 97, 141–197.

Riedinger, N., Pfeifer, K., Kasten, S., Garming, L.F.L., Vogt, C., Hensen, C., 2005. Diagenetic alteration of magnetic signals by anaerobic oxidation of methane related to a change in sedimentation rate. Geochim. Cosmochim. Acta 69, 4117–4126.

Roberts, A.P., 1995. Magnetic properties of sedimentary greigite ($Fe_3S_4$). Earth Planet. Sci. Lett. 134, 227–236.

Roberts, A.P., Weaver, R., 2005. Multiple mechanisms of remagnetization involving sedimentary greigite ($Fe_3S_4$). Earth Planet. Sci. Lett. 231, 263–277.

Roberts, A.P., Pike, C.R., Verosub, K.L., 2000. First-order reversal curve diagrams: a new tool for characterizing magnetic properties of natural samples. J. Geophys. Res. 105, 28461–28475.

Roberts, A.P., Liu, Q.S., Rowan, C.J., Chang, L., Carvallo, C., Torrent, J., Horng, C.S., 2006. Characterization of hematite ($\alpha$-$Fe_2O_3$), goethite ($\alpha$-FeOOH), greigite ($Fe_3S_4$), and pyrrhotite ($Fe_7S_8$) using first-order reversal curve diagrams. J. Geophys. Res. 111, B12S35. doi:10.1029/2006JB004715.

Rowan, C.J., Roberts, A.P., 2005. Tectonic and geochronological implications of variably timed magnetizations carried by authigenic greigite in marine sediments from New Zealand. Geology 33, 553–556.

Rowan, C.J., Roberts, A.P., 2006. Magnetite dissolution, diachronous greigite formation, and secondary magnetizations from pyrite oxidation: unravelling complex magnetizations in Neogene marine sediments from New Zealand. Earth Planet. Sci. Lett. 241, 119–137.

Sagnotti, L., Roberts, A.P., Weaver, R., Verosub, K.L., Florindo, F., Pike, C.R., Clayton, T., Wilson, G.S., 2005. Apparent magnetic polarity reversals due to remagnetization resulting from late diagenetic growth of greigite from siderite. Geophys. J. Int. 100, 89–100.

Schoonen, M., Smirnov, A., Cohn, C., 2004. A perspective on the role of minerals in prebiotic synthesis. Ambio 33, 539–551.

Snowball, I.F., 1991. Magnetic hysteresis properties of greigite ($Fe_3S_4$) and a new occurrence in Holocene sediments from Swedish Lappland. Phys. Earth Planet. Inter. 68, 32–40.

Torres, M.E., Rugh, W.D., 2006. Data report: isotopic characterization of dissolved inorganic carbon in pore waters, Leg 204. In: Tréhu, A.M., Bohrmann, G., Torres, M.E., Colwell, F.S. (Eds.), Proc. ODP, Sci. Res., vol. 204. Ocean Drilling Program, College Station, TX, pp. 1–16. doi:10.2973/odp.proc.sr.204.117.2006.

Tréhu, A.M., Bohrmann, G., Rack, F.R., Torres, M.E., et al., 2003. Proc. ODP, Init. Repts., vol. 204. Ocean Drilling Program, College Station, TX. doi:10.2973/odp.proc.ir.204.2003.

Tréhu, A.M., Long, P.E., Torres, M.E., Bohrmann, G., Rack, F.R., Collett, T.S., Goldberg, D.S., Milkov, A.V., Riedel, M., Schultheiss, P., Bangs, N.L., Barr, S.R., Borowski, W.S., Claypool, G.E., Delwiche, M.E., Dickens, G.R., Gràcia, E., Guerin, G., Holland, M., Johnson, J.E., Lee, Y.J., Liu, C.S., Su, X., Teichert, B., Tomaru, H., Vanneste, M.E., Watanabe, M., Weinberger, J.L., 2004a. Three-dimensional distribution of gas hydrate beneath southern Hydrate Ridge: constraints from ODP Leg 204. Earth Planet. Sci. Lett. 222, 845–862.

Tréhu, A.M., Flemings, P.B., Bangs, N.L., Chevallier, J., Gràcia, E., Johnson, J.E., Liu, C.S., Riedel, M., Torres, M.E., 2004b. Feeding methane vents and gas hydrate deposits at south Hydrate Ridge. Geophys. Res. Lett. 31, L23310. doi:10.1029/2004GL021286.

Tréhu, A.M., Torres, M.E., Bohrmann, G., Colwell, F.S., 2006. Leg 204 synthesis: gas hydrate distribution and dynamics in the central Cascadia accretionary complex. In: Tréhu, A.M., Bohrmann, G., Torres, M.E., Colwell, F.S. (Eds.), Proc. ODP, Sci. Res., vol. 204. Ocean Drilling Program, , College Station, TX, pp. 1–41. doi:10.2973/odp.proc.sr.204.101.2006.

Weaver, R., Roberts, A.P., Barker, A.J., 2002. A late diagenetic (syn-folding) magnetization carried by pyrrhotite: implications for paleomagnetic studies from magnetic iron sulphide-bearing sediments. Earth Planet. Sci. Lett. 200, 371–386.

Wehland, F., Stancu, A., Rochette, P., Dekkers, M.J., Appel, E., 2005. Experimental evaluation of magnetic interaction in pyrrhotite-bearing samples. Phys. Earth Planet. Inter. 153, 181–190.

Weinberger, J.L., Brown, K.M., Long, P., 2005. Painting a picture of gas hydrate distribution with thermal images. Geophys. Res. Lett. 32, L04609. doi:10.1029/2004GL021437.

Wellsbury, P., Goodman, K., Cragg, B.A., Parkes, R.J., 2000. The geomicrobiology of deep marine sediments from Blake Ridge containing methane hydrate (Sites 994, 995, and 997). In: Paul, C.K., Matsumoto, R., Wallace, P.J., Dillon, W.P. (Eds.), Proc. ODP Sci. Res., vol. 164. Ocean Drilling Program, College Station, TX, pp. 379–391.